

Supplementary Materials for

A global monthly field of seawater pH over 3 decades: a machine learning approach

Guorong Zhong, Xuegang Li, Jinming Song, Baoxiao Qu, Fan Wang, Yanjun Wang, Bin Zhang, Lijing Cheng, Jun Ma, Huamao Yuan, Liqin Duan, Ning Li, Qidong Wang, Jianwei Xing, Jiajia Dai

Corresponding author: lixuegang@qdio.ac.cn and jmsong@qdio.ac.cn

The PDF file includes:

Supplementary Text
Figs. S1 to S2
Tables S1

Supplementary Text

Uncertainty and construction method of selected ocean products

A group of products related to the physical, chemical, and biological activities that influence the ocean carbonate system were collected as potential pH predictors (Table 1). These products were constructed using different methods in previous research. The seawater temperature and salinity product were constructed based on measurements from the World Ocean Database (WOD) using the ensemble optimal interpolation method with the dynamic ensemble (EnOI-DE) provided by CMIP5 historical simulations (Cheng et al., 2016; Cheng et al., 2020). The temperature product was claimed with an uncertainty of about $\pm 0.05^{\circ}\text{C}$ in the recent few decades, and the uncertainty of salinity product was about $\pm 0.001 \sim \pm 0.005$ at different depths (present as figures in Cheng et al., 2016 and Cheng et al., 2020; <https://journals.ametsoc.org/view/journals/clim/33/23/full-jcliD200366-f5.jpg> and <https://journals.ametsoc.org/view/journals/clim/29/15/full-jcli-d-15-0730.1-f8.jpg>).

The climatological Alk product was constructed from Global Ocean Data Analysis Project version 2.2019 (GLODAPv2019) measurements using a neural network (NNGv2) method, with the RMSE of $3\text{--}6.2 \mu\text{mol kg}^{-1}$ (Broullón et al., 2019). The climatological DIC product was constructed from GLODAPv2019 and the Lamont–Doherty Earth Observatory (LDEO) datasets using a feedforward neural network

37 (dubbed NNGv2LDEO) method, with a RMSE of 3.6–13.2 $\mu\text{mol kg}^{-1}$ (Broullón et al.,
38 2020). The climatological dissolved oxygen, nitrate, phosphate, and silicate product
39 was constructed based on measurements from the World Ocean Database, using an
40 objective analysis method that generated a first-guess field and then carried out a
41 correction at all gridpoints as a distance-weighted mean of all gridpoint difference
42 values that lie within the area around the gridpoint defined by the influence radius
43 (Gracia et al., 2020a; Gracia et al., 2020b). The producer claimed an average DO bias
44 of $0.4\pm 4.7 \mu\text{mol kg}^{-1}$ below 500 m depth and $1.4\pm 10.9 \mu\text{mol kg}^{-1}$ above 500 m depth.
45 The average biases of nutrient concentration were $-0.02\pm 0.07 \mu\text{mol kg}^{-1}$ for phosphate,
46 $-0.22\pm 0.95 \mu\text{mol kg}^{-1}$ for nitrate, and $-0.3\pm 3.8 \mu\text{mol kg}^{-1}$ for silicate below 500 m depth,
47 and were $0.01\pm 0.12 \mu\text{mol kg}^{-1}$ for phosphate, $0.2\pm 1.8 \mu\text{mol kg}^{-1}$ for nitrate, and 0.8 ± 3.6
48 $\mu\text{mol kg}^{-1}$ for silicate above 500 m depth. The Sea surface height (SSH), mixed layer
49 depth (MLD), and W velocity of ocean current from the ECCO2 cube92 product were
50 constructed by least squares fit of a global full-depth-ocean and sea-ice configuration
51 of the Massachusetts Institute of Technology general circulation model to the available
52 satellite and in-situ data (Menemenlis et al., 2008). The basin-wide median bias error
53 of the MLD product is -6.6 m and the RMSE is 40 m, and the RMSE of the SSH product
54 is 9.2 cm. The ERA5 sea level pressure and surface pressure were constructed by the
55 Integrated Forecasting System (IFS) Cy41r2 model (Hersbach et al., 2020). The
56 standard deviation of ERA5 sea level pressure and surface pressure are within 1 hPa
57 and 0.8 hPa in the recent three decades. The NOAA Greenhouse Gas Marine Boundary
58 Layer Reference xCO_2 product is constructed by extending measurements from a subset
59 of sites from the NOAA Cooperative Global Air Sampling Network, with an uncertainty
60 within $1 \mu\text{mol mol}^{-1}$ in most regions (Lan et al., 2023,
61 <https://gml.noaa.gov/ccgg/mbl/mbl.html>). The bi-monthly Multivariate El
62 Niño/Southern Oscillation index (MEI) was calculated by the first seasonally varying
63 principal component of six atmosphere–ocean (COADS) variable fields in the tropical
64 Pacific basin (Wolter et al., 2011). The Arctic Oscillation index was calculated as the
65 first leading mode from the Empirical Orthogonal Function analysis of monthly mean
66 height anomalies at 1000-hPa of the Northern Hemisphere or 700-hPa of the Southern
67 Hemisphere (CPC, 2002). The Southern Oscillation Index was calculated based on the
68 differences in air pressure anomaly between Tahiti and Darwin, Australia (CPC, 2005).
69 The specific uncertainty of these index products is not provided. The GEBCO global
70 bathymetric data was constructed using predicted depths based on the V32 gravity

71 model (Sandwell et al., 2019). The monthly surface ocean $p\text{CO}_2$ was constructed using
72 the SOM-FFNN method based on regional-specific predictors selected by the stepwise
73 FFNN algorithm, with a global RMSE of 17.99 μatm (Zhong et al., 2022). A
74 climatological $p\text{CO}_2$ product constructed by another SOM-FFNN model was also used,
75 with the RMSE of 18.3 μatm (Landschützer et al., 2020). The Euphotic Depth product
76 was constructed from remote sensing reflectance (RRS) data derived inherent optical
77 properties using Lee algorithm (Lee et al., 2007), with an average percentage error of
78 13.7%. The chlorophyll concentration product was constructed based on RRS at 2-4
79 wavelengths between 440 and 670 nm with an uncertainty of 1-2%, using the algorithm
80 of Hu et al. (2019) that combines an empirical band difference approach at low
81 chlorophyll concentrations with a band ratio approach at higher chlorophyll
82 concentrations. The photosynthetically available radiation (PAR) product was based on
83 the observed Top-of-Atmosphere (TOA) radiances in the 400-700nm range that do not
84 saturate over clouds using the algorithm of Frouin et al. (2002), with an RMSE of 3.6
85 Einstein/ m^2/day . The product of the diffuse attenuation coefficient at 490 nm (K_d490)
86 was calculated using an empirical relationship derived from in situ measurements
87 of K_d490 and blue-to-green band ratios of RRS. The remote sensing reflectance
88 product was derived from ocean color sensors based on the spectral distribution of
89 reflected visible solar radiation upwelling from below the ocean surface and passing
90 through the sea-air interface. The total absorption and backscattering products were
91 calculated using the default global configuration of the Generalized Inherent Optical
92 Property (GIOP) model (Werdell et al., 2013).

93 Validation of cross-boundary method

94 The cross-boundary method reduced the pH predicting error slightly, but improved
95 the discontinuity problem in the SOM boundary effectively (Figure S1 a-d). However,
96 the discontinuity problem was not completely solved and some boundary line existed
97 in the spatial distribution, especially in the deeper ocean that pH measurements are
98 much sparser (Figure S1 e-f). Even so, the performance of FFNN predicting was better
99 when the cross-boundary method was applied. Compared with taking average in the
100 boundary area, the cross-boundary method avoided subjectively modifying the
101 boundary data. Correspondingly, this method may not solve the discontinuity problem
102 perfectly in some situations. The cross-boundary method also decreased the
103 predicting error slightly in vertical boundary areas (2 layers near the mixed layer depth).
104 However, the improvement was minor in the vertical distribution, due to the natural

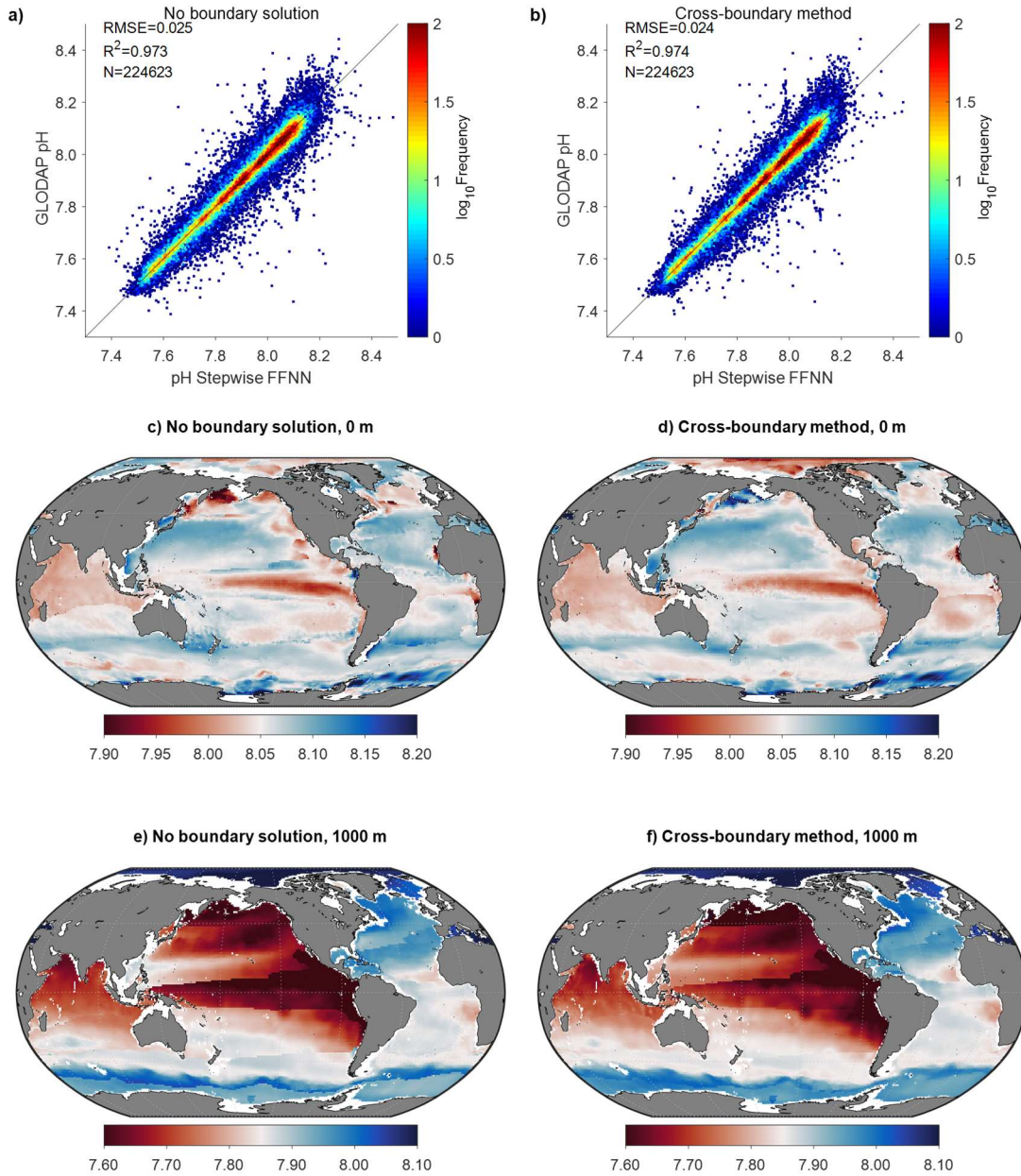
105 existing substantial vertical gradient of seawater pH near the mixed layer depth (Figure
106 S2). Overall, the cross-boundary method increases information about seawater pH
107 variation out of boundaries in the neural network learning process, reducing the outliers
108 near the SOM boundary and vertical boundary.

109

110 **Fig. S1. Validation of cross-boundary method for pH predicting in the SOM boundary. a-b):**

111 comparison of FFNN predicted pH with GLODAP in all SOM boundary areas; c-f): comparison

112 of spatial distribution at 0 m and 1000 m in January 2020.



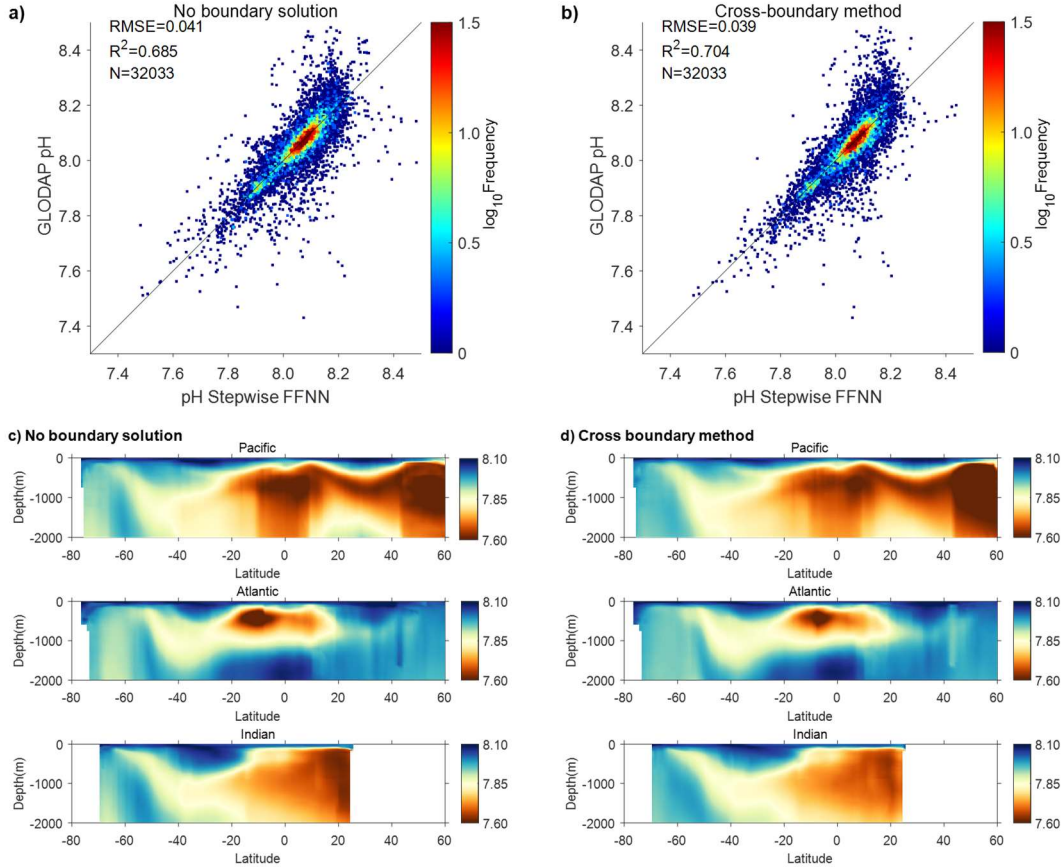
113

114

115

116

117 **Fig. S2. Validation of cross-boundary method for pH predicting in the vertical boundary.** a)
 118 and b): comparison of FFNN predicted pH with GLODAP in all vertical boundary areas (2 layers
 119 near the mixed layer depth); c) and d): comparison of vertical distribution at different basin in
 120 January 2020.



121

122

123 **Table. S1. Predictors selected by the stepwise FFNN algorithm in the Mixed layer for period**
 124 **before August 2002.** The predictors are arranged in order of relative importance, with the
 125 variables listed at the front of each province being more effective in reducing predicting errors
 126 when used as pH predictors.

Province	FFNN neurons	Predictors
P5 Equatorial Atlantic	25	Phosphate, Temp, SLP, DIC, P_{surf} , TA, pCO_2 , $W_{vel}(in-situ)$, DO
P8 Equatorial Pacific	10	pCO_2 , Depth, sLat, Temp, Sal, DIC, $W_{vel}(in-situ)$, Nitrate
P10 Subtropical South Atlantic	20	pCO_2 , Silicate, Nitrate, $W_{vel}(65m)$, $W_{vel}(195m)$
P11 Subtropical South Pacific	10	Phosphate, pCO_2 , Depth, sLat, Silicate, pCO_2_{clim} , $W_{vel}(5m)$, $W_{vel}(105m)$

127

128

129

130 **References mentioned in supplementary text:**

- 131 Broullón, D., Pérez, F. F., Velo, A., Hoppema, M., Olsen, A., Takahashi, T., ... & van
132 Heuven, S. M. A global monthly climatology of total alkalinity: a neural network
133 approach. *Earth System Science Data*, 11, 1109-1127 (2019).
- 134 Broullón, D., Pérez, F. F., Velo, A., Hoppema, M., Olsen, A., Takahashi, T., ... & Kozyr,
135 A. A global monthly climatology of oceanic total dissolved inorganic carbon: a
136 neural network approach. *Earth System Science Data*, 12, 1725-1743 (2020).
- 137 Cheng, L., & Zhu, J. Benefits of CMIP5 multimodel ensemble in reconstructing
138 historical ocean subsurface temperature variations. *Journal of Climate*, 29, 5393-
139 5416 (2016).
- 140 Cheng, L., Trenberth, K. E., Gruber, N., Abraham, J. P., Fasullo, J. T., Li, G., ... & Zhu,
141 J. Improved estimates of changes in upper ocean salinity and the hydrological
142 cycle. *Journal of Climate*, 33, 10357-10381 (2020).
- 143 Climate Prediction Center. Daily Arctic Oscillation Index. [Accessed on 2021/08/20].
144 [https://www.cpc.ncep.noaa.gov/products/precip/CWlink/daily_ao_index/ao_index.](https://www.cpc.ncep.noaa.gov/products/precip/CWlink/daily_ao_index/ao_index.html)
145 [html](https://www.cpc.ncep.noaa.gov/products/precip/CWlink/daily_ao_index/ao_index.html). (2002).
- 146 Climate Prediction Center. Southern Oscillation Index. [Accessed on 2021/08/20].
147 https://www.cpc.ncep.noaa.gov/products/analysis_monitoring/ensocycle/soi.shtml.
148 (2005).
- 149 Frouin, R., Franz, B. A., & Werdell, P. J. (2002). The SeaWiFS PAR product. ,In: S.B.
150 Hooker and E.R. Firestone, Algorithm Updates for the Fourth SeaWiFS Data
151 Reprocessing, NASA Tech. Memo. 2003-206892, Volume 22, NASA Goddard
152 Space Flight Center, Greenbelt, Maryland, 46-50.
- 153 Garcia, H. E., Weathers, K. W., Paver, C. R., Smolyar, I., Boyer, T. P., Locarnini, M.
154 M., ... & Seidov, D. *World Ocean Atlas 2018, Volume 3: Dissolved Oxygen,*
155 *Apparent Oxygen Utilization, and Dissolved Oxygen Saturation* (2019).
- 156 Garcia, H. E., Weathers, K. W., Paver, C. R., Smolyar, I., Boyer, T. P., Locarnini, M.
157 M., ... & Seidov, D. *World ocean atlas 2018. Vol. 4: Dissolved inorganic nutrients*
158 *(phosphate, nitrate and nitrate+ nitrite, silicate)* (2019).
- 159 Hersbach, H., Bell, B., Berrisford, P., Hirahara, S., Horányi, A., Muñoz-Sabater, J., ...
160 & Thépaut, J. N. The ERA5 global reanalysis. *Quarterly Journal of the Royal*
161 *Meteorological Society*, 146(730), 1999-2049 (2020).
- 162 Hu, C., Feng, L., Lee, Z., Franz, B. A., Bailey, S. W., Werdell, P. J., & Proctor, C. W.
163 Improving satellite global chlorophyll a data products through algorithm refinement
164 and data recovery. *Journal of Geophysical Research: Oceans*, 124(3), 1524-1543
165 (2019).
- 166 Lan, X., Tans, P. & K.W. Thoning. Trends in globally-averaged CO₂ determined from
167 NOAA Global Monitoring Laboratory measurements.
168 <https://gml.noaa.gov/ccgg/trends/> (2023).
- 169 Landschützer, P., Laruelle, G. G., Roobaert, A., & Regnier, P. A uniform pCO₂
170 climatology combining open and coastal oceans. *Earth System Science Data*, 12,
171 2537-2553 (2020).

172 Lee, Z., Weidemann, A., Kindle, J., Arnone, R., Carder, K. L., & Davis, C. Euphotic
173 zone depth: Its derivation and implication to ocean-color remote sensing. *Journal of*
174 *Geophysical Research*, 112(C3) (2007).

175 Menemenlis, D., Campin, J. M., Heimbach, P., Hill, C., Lee, T., Nguyen, A., ... &
176 Zhang, H. ECCO2: High resolution global ocean and sea ice data synthesis. *Mercator*
177 *Ocean Quarterly Newsletter*, 31, 13-21 (2008).

178 Sandwell, D. T., Harper, H., Tozer, B., & Smith, W. H. Gravity field recovery from
179 geodetic altimeter missions. *Advances in Space Research*, 68(2), 1059-1072 (2021).

180 Werdell, P. J., Franz, B. A., Bailey, S. W., Feldman, G. C., Boss, E., Brando, V. E., ...
181 Mangin, A. Generalized ocean color inversion model for retrieving marine inherent
182 optical properties. *Applied Optics*, 52(10), 2019 (2013).

183 Wolter, K., & Timlin, M. S. El Niño/Southern Oscillation behaviour since 1871 as
184 diagnosed in an extended multivariate ENSO index (MEI. ext). *International Journal*
185 *of Climatology*, 31, 1074-1087 (2011).

186 Zhong, G., Li, X., Song, J., Qu, B., Wang, F., Wang, Y., ... & Duan, L. Reconstruction
187 of global surface ocean pCO₂ using region-specific predictors based on a stepwise
188 FFNN regression algorithm. *Biogeosciences*, 19, 845-859 (2022).